Palaeogeography, Palaeoclimatology, Palaeoecology 440 (2015) 725–733

Contents lists available at ScienceDirect

Palaeogeography, Palaeoclimatology, Palaeoecology

journal homepage: www.elsevier.com/locate/palaeo

Volcanism and deep-ocean acidification across the end-Triassic extinction event

Masayuki Ikeda [a,*], Rie S. Hori [b], Yuki Okada [b], Ryoichi Nakada [c,d]

[a] Graduate school of Geoscience, Shizuoka University, Shizuoka, Shizuoka 422-8529, Japan
[b] Department of Earth Sciences, Graduate School of Science and Engineering, Ehime University, Matsuyama, Ehime 790-8577, Japan
[c] Earth-Life Science Institute, Tokyo Institute of Technology, Meguro, Tokyo 152-8550, Japan
[d] Kochi Institute for Core Sample Research, Japan Agency for Marine-Earth Science and Technology (JAMSTEC), Nankoku, Kochi 783-8502, Japan

ARTICLE INFO

Article history:
Received 3 March 2015
Received in revised form 21 September 2015
Accepted 25 September 2015
Available online 9 October 2015

Keywords:
Acidification
Triassic–Jurassic
Central Atlantic magmatic province (CAMP)
Bedded chert
Aeolian dust
Extinction

ABSTRACT

The end-Triassic extinction event marks one of the "big five" mass extinction events of the Phanerozoic. The ultimate cause of the extinction is considered to be volcanic activity at the Central Atlantic magmatic province (CAMP), yet the underlying nature of global environmental changes that accompanied the biotic turnover remains elusive. Here we present chemical and mineralogical studies across the end-Triassic extinction level of the deep-sea chert sequence (Inuyama, Japan). Depleted hematite content normalized by terrigenous material predated the end-Triassic extinction level with significant rock color change from brick red to purple, which is consistent with the rock magnetic records of hematite reported. This suggests the loss of authigenic hematite possibly due to the acidification of bottom-water and the underlying sediment pore-water. This timing is consistent with the initial eruption of CAMP volcanism, suggesting a catastrophic release of greenhouse gases as a cause of deep-ocean acidification. Across the end-Triassic extinction interval, MgO/Al_2O_3, Fe_2O_3/Al_2O_3, and Al_2O_3/SiO_2 increased with change in color from purple to dusty red. This trend became close to those of weathered CAMP basalts in arid area, implying that it became the considerable source of aeolian dust in cherts after the end-Triassic extinction event. These temporal relations support the synchrony among the initial eruption of CAMP, deep-ocean acidification, and the end-Triassic extinction. Similar rock color changes of cherts might have potential information for the volcanisms and deep-ocean acidification in other geologic events.

1. Introduction

The Triassic–Jurassic (T–J) extinction event (~201.5 Ma; Blackburn et al., 2013) is one of the "big five" mass extinction events of the Phanerozoic (e.g. Raup and Sepkoski, 1982; Hallam, 2002). This event was caused by the massive emissions of CO_2 and other volatiles associated with the eruption of the Central Atlantic magmatic province (CAMP) (e.g. Marzoli et al., 1999; Schaller et al., 2011). The release of CO_2 and volatiles from the CAMP flood basalts could have produced ocean acidification event, which was suggested as a key causal mechanism of the end-Triassic extinction (e.g. Abrajevitch et al., 2013; Bacon et al., 2013; Greene et al., 2012; Tanner et al., 2004; van de Schootbrugge et al., 2009).

Double-phased deep-ocean acidification event was suggested based on the variations in the relative abundances and characteristics of magnetic records of deep-sea chert in Japan (Abrajevitch et al., 2013). The initial stage, characterized by a disappearance of the previously ubiquitous magnetite (inorganic remains of magnetotactic bacteria), started ~100–120 kyr prior to the end-Triassic extinction. The second stage, defined by significant changes magnetic properties of hematite pigment, lasted ~15–35 kyr until the end-Triassic extinction.

However, these timings are inconsistent with the current consensus of synchronous between the end-Triassic extinction and CAMP volcanism within 20 kyr-order (Blackburn et al., 2013; Deenen et al., 2010; Whiteside et al., 2007, 2010). In addition, rock magnetic records of chert should have reflected not only depositional environmental, but also diagenetic effects after deposition and changes in component of aeolian input, which could have reflected the widespread eruption of CAMP flood basalts.

To examine these effects, we here examine the quantitative mineralogical and chemical compositions of cherts by using X-ray absorption fine structure (XAFS) and XRF. XAFS analysis of Fe is a powerful method to determine iron species in chert in the Inuyama area, as recently performed by Nakada et al. (2014), because the identification of Fe-bearing minerals in chert is not easy due to low Fe concentration in chert (e.g., Murray et al., 1991; Murray, 1994). Based on the XAFS in addition to recently reported chemical composition results (Okada et al., 2015), we discuss the paleoclimatic/paleoceanographic changes across the end-Triassic extinction, from the viewpoints of deep-ocean acidification and CAMP volcanic activity.

* Corresponding author.
E-mail address: ikeda.masayuki@shizuoka.ac.jp (M. Ikeda).

http://dx.doi.org/10.1016/j.palaeo.2015.09.046
0031-0182/

2. Geologic setting

Studied sections are located at the Katsuyama, in the Inuyama area, southwestern part of the Mino Terrane, central Japan (Fig. 1). The Mino Terrane is a Paleozoic to Mesozoic accretionary complex consisting of greenstone, limestone, bedded chert, and siliciclastic rocks (Wakita, 1988). The accretionary complex exposed in the Inuyama area comprises the Lower Triassic siliceous mudstone, Lower Triassic to Lower Jurassic bedded chert, and Lower to Upper Jurassic siliciclastic rocks, which are repeated as tectonic slices (Fig. 1; Matsuda and Isozaki, 1991; Yao et al., 1980, Kimura and Hori, 1993). The siliceous mudstone and bedded chert sequences were deposited on the pelagic deep-sea floor of Panthalassa superocean below carbonate compensation depth (CCD), whereas siliciclastic rocks are considered to have been deposited on hemipelagic deep-sea and within a trench in a subduction zone (Matsuda and Isozaki, 1991). Paleomagnetic and biostratigraphic studies of the bedded chert sequence in the Inuyama area show that the site of deposition moved from low latitudes during the Middle Triassic to mid-latitudes during the Lower Jurassic (Fig. 1; Shibuya and Sasajima, 1986; Oda and Suzuki, 2000; Ando et al., 2001).

The bedded chert sequence consists of rhythmically alternation of cm-thick chert and mm-thick shale beds in this area. The chert beds are SiO_2-diluted parts of the shale beds and, consist mainly of biogenic silica and continental materials, such as aeolian dusts derived from the continental surface (e.g. Hori et al., 1993, 2000). Alternating chert and shale beds are considered to be the result of the precession-scale changes in the accumulation rate of biogenic SiO_2 in environments with ca. 100 times slower accumulation of terrigenous material with probable aeolian dust (e.g. Hori et al., 1993).

Across the end-Triassic extinction interval, there is no evidence for a major lithological change, except for distinct color variations from brick red to dusty red (Carter and Hori, 2005; Hori, 1992; Okada et al., 2015). The top of the uppermost brick red chert and the overlain two chert beds are purple in color. Shale thickness increased across the end-Triassic extinction (Fig. 2; Sugiyama, 1997; Ikeda and Tada, 2013). These lithologic changes could have reflected by paleoenvironmental changes across end-Triassic extinction interval.

2.1. Chronostratigraphy of T–J deep-sea chert sequence

Chronostratigraphy of T–J deep-sea sequence in the Inuyama area has been revised after well-established radiolarian–conodont biostratigraphy and cyclostratigraphy (Hori, 1988, 1990; Sugiyama, 1997; Carter and Hori, 2005; Ikeda and Tada, 2013). The end-Triassic radiolarian extinction interval is well constrained within a lowermost dusty red chert based on the last appearance datum (LAD) of Triassic radiolarian *Globolaxtorum tozeri* assemblage and conodont *Misikella posthernsteini*, and the first appearance datum (FAD) occurrence of Jurassic radiolarian *Pantanellium tanuense* (Carter and Hori, 2005; Hori, 1992). Similar radiolarian faunal change across the end-Triassic extinction interval was found within the interval of less than 5 m at the shallow marine sequence in the Queen Charlotte Islands (Fig. 3; Carter and Hori, 2005) and the New York Canyon. In the Queen Charlotte Islands and New York Canyon, the LAD of Triassic-type radiolarians and conodont are at the LAD of Triassic ammonoid *Choristoceras rhaeticum* (Ward et al., 2004; Orchard et al., 2007), and the FAD of Jurassic-type radiolarian is 7 m below the first occurrence of Jurassic ammonoid *Psiloceras* aff. *primocostatum* (Fig. 3; Tipper and Guex, 1994; Ward et al., 2004).

The age of the end-Triassic radiolarian extinction event can be constrained as 201.4 ± 0.2 Ma on the basis of 201.33 ± 0.13 Ma and 201.45 ± 0.14 Ma of the U–Pb ages from the New York Canyon section, U. S. A. and Pucara section, Peru, respectively (Fig. 3; Schoene et al., 2010; Guex et al., 2012). 201.33 ± 0.13 Ma of U–Pb age was measured from NYC-N10 ash bed, which level is 1 m above the LAD of Jurassic ammonoid *Ps. spelae* at the New York Canyon (Fig. 3; Schoene et al., 2010). 201.45 ± 0.14 Ma of U–Pb age was measured from the ash bed LM4–86, which level is 1.5 m above the LAD of Triassic ammonoid *Ch. crickmayi* and 4.5 m below the FAD of *Ps. spelae* at the Pucara (Fig. 3; Guex et al., 2012). The horizons of the end-Triassic ammonoid extinction and earliest Jurassic ammonoid recovery at New York Canyon and Pucara sections can be correlated with those horizons at the Queen Charlotte Islands, respectively (e.g. Guex et al., 2004, 2008; Ward et al., 2001, 2004, 2007). Therefore, the end-Triassic radiolarian extinction intereval in the Inuyama area can be estimated as 201.4 ± 0.2 Ma, which errors from 201.45 ± 0.14 Ma and 201.33 ± 0.13 Ma of U–Pb ages (Fig. 3).

Milankovitch-scale astronomical cycles have been linked to the sedimentary rhythms of the bedded chert (e.g. Hori et al., 1993; Ikeda and Hori, 2014; Ikeda and Tada, 2013, 2014; Ikeda et al., 2010). Hierarchal cyclicities corresponding to the 40 kyr obliquity cycle and ~100 kyr, 405 kyr, ~2000 kyr, and ~4000 kyr eccentricity cycles have been identified from chert thickness variations in the Lower Triassic to Lower Jurassic bedded chert sequence in the Inuyama area (e.g. Ikeda and Tada, 2014). The astrochronology for the Upper Triassic to Lower Jurassic bedded chert sequences at the Katsuyama section has been established

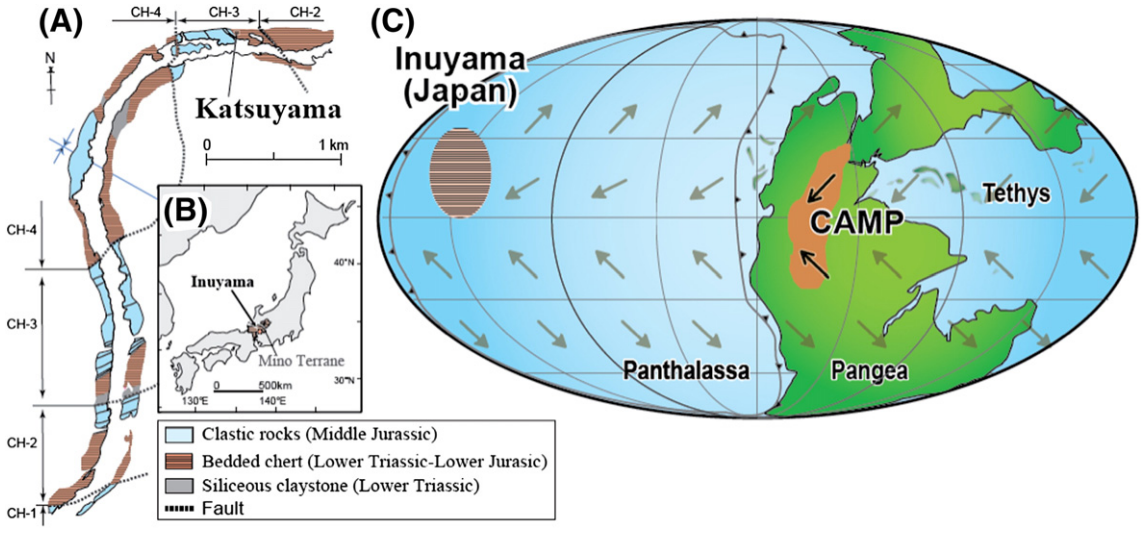

Fig. 1. (A) A geologic map and (B) a location map showing the locations of Katsuyama and Sakahogi sections in the Inuyama area, Mino–Tanba Terrane, Japan. (C) A palaeogeographic map during Triassic–Jurassic transition showing the locality of the Inuyama area (red zone; Shibuya and Sasajima, 1986; Oda and Suzuki, 2000; Ando et al., 2001). Base map is after Scotese and Langford (1995). The arrows and brown zone suggest the estimated surface winds and the distribution of the Central Atlantic magmatic province (CAMP; Kent and Tauxe, 2005; Whiteside et al., 2010).

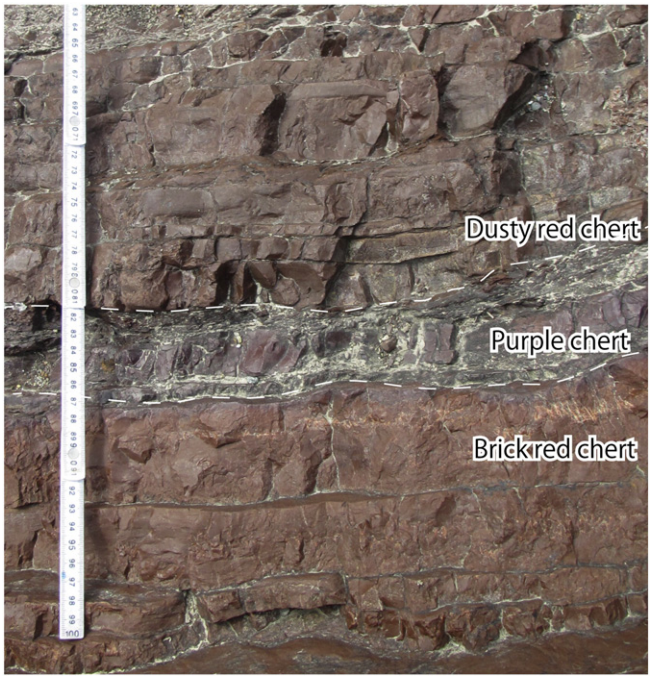

Fig. 2. Photo of Triassic–Jurassic transition showing the distinct color change from dusty red to brown red chert intercalated with purple chert bed between the two.

primary based on each chert-shale couplet being linked to the ~20 kyr precession cycle, and then fine-tuned by linking ~20 bed cycles to 405 kyr eccentricity cycles (Ikeda and Tada, 2013, 2014). The astrochronology of the Inuyama deep-sea sequence was anchored at the end-Triassic radiolarian extinction event as 201.4 ± 0.2 Ma, as describe above.

3. Analytical methods

Across the end-Triassic extinction interval, 12 samples were analyzed for XAFS. All chert samples were crushed into small pieces and sorted to avoid veinlets and stains due to surface weathering. After careful washing with Milli-Q (Millipore) water, the pieces were air-dried and then powdered using an agate planetary mill in preparation for XRF and XAFS geochemical analyses (Okada et al., 2015). The XRF analytical method and sample preparation for cherts were modified from Higuchi and Hori (1996), Hori and Higuchi (1996), and Yoshizaki et al. (1996).

3.1. X-ray absorption fine structure (XAFS) analysis

X-ray absorption fine structure (XAFS) is a powerful tool used to determine the electronic structure and the neighboring elements from X-ray absorption. The XAFS spectrum is divided into two energy regions: X-ray absorption near-edge structure (XANES) and extended X-ray absorption edge structure (EXAFS). The former gives information about electronic states (valence) and the symmetry of the coordination environment. The latter is sensitive to the local structure of the center atom absorbing the incident X-ray (Fe in this case), including the interatomic distances and coordination numbers of the neighboring atoms. Although XANES spectra are useful for the qualitative identification of major classes such as distinguishing among sulfides, carbonate, phosphates, phyllosilicates, oxides, and oxyhydroxides, EXAFS is more sensitive to detect a particular component at low abundance (O'Day et al., 2004).

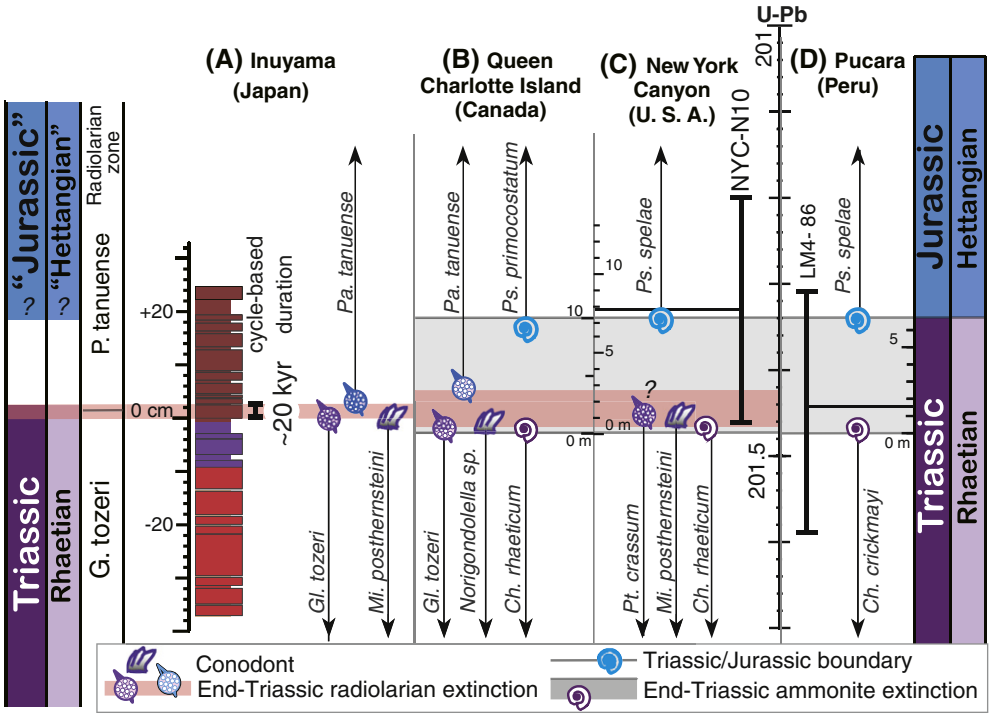

Fig. 3. Radiolarian and conodont biostratigraphic correlation of (A) the uppermost Triassic to lowermost Jurassic deep-sea sequence in the Inuyama area, central Japan (Carter and Hori, 2005; Ikeda and Tada, 2013; Okada et al., 2015) with the shallow marine sections in (B) Queen Charlotte Island, Canada (Carter and Hori, 2005; Carter et al., 2010; Tipper and Guex, 1994; Williford et al., 2007) and (C) New York Canyon, U. S. A (Orchard et al., 2007). Ammonoid biostratigraphic correlation among the shallow marine sections in Queen Charlotte Island, New York Canyon (Guex et al., 2012; 2004; 2008; Ward et al., 2001, 2004, 2007; Williford et al., 2007), and (D) Pucara section, Peru (e.g. Schaltegger et al., 2008; Schoene et al., 2010; Guex et al., 2012) are also shown. The astronomical time scale of Inuyama bedded chert (Inuyama-ATS) is anchored at the base of dusty red chert bed number 796 as the end-Triassic radiolarian extinction (201.40 ± 0.20 Ma; Ikeda and Tada, 2013).

The Fe K-edge (7111 eV) EXAFS spectra were measured at BL-01B1 of SPring-8 (Hyogo, Japan). Prior to the measurements, the X-ray energy was calibrated with the pre-edge peak maximum of hematite at 7114 eV. The EXAFS spectra of the reference materials, hematite, illite, magnetite, Fe-phosphate, chlorite, hornblende, biotite, smectite, ferrihydrite, goethite, and pyrite, were measured in the transmission mode (Fig. 4), while the spectra of chert samples were measured in the fluorescence mode using a 19-element germanium (Ge) semiconductor detector (Fig. 5). Clay minerals, including illite (IMt-1), smectite (SWy-2), and chlorite (CCa-2), were obtained from the Source Clays Repository of the Clay Mineral Society, USA. After dry sieving, clay standards with grain sizes smaller than 20 μm were obtained. Minerals such as biotite, pyrite (FeS_2), and hornblende were obtained from Nichika Inc. (Kyoto, Japan). Magnetite (Fe_3O_4) was obtained from Wako Pure Chemical Industries Ltd. Ferrihydrite, goethite and hematite were synthesized following the method of Schwertmann and Cornell (2000), while the Fe-phosphate was synthesized following the method of Voegelin et al. (2010). The measurements were conducted at ambient pressure and temperature. The EXAFS spectra were analyzed using Athena software (Ravel and Newville, 2005). The energy unit was transformed from eV to $Å^{-1}$ to produce the EXAFS function $\chi(k)$, where k ($Å^{-1}$) is the photoelectron wave vector. The contributions of the various Fe species in each sample were estimated by linear combination fitting (LCF) of each k^3-weighted EXAFS spectrum with the spectra of the reference materials. The LCF was conducted using no more than three minerals in a k range of 2–11.5 $Å^{-1}$. The quality of the fit was given by the residual value, the goodness-of-fit parameter R, defined by

$$R = \frac{\sum \left[k^3\chi_{obs}(k) - k^3\chi_{cal}(k)\right]^2}{\sum \left[k^3\chi_{obs}(k)\right]^2} \quad (1)$$

where $\chi_{obs}(k)$ and $\chi_{cal}(k)$ are the experimental and calculated absorption coefficients at a given k, respectively, and a smaller R value means a better fit in the LCF procedure.

4. Results

4.1. Changes in Fe-bearing mineral contents across the end-Triassic extinction interval

All the cherts require hematite and illite with magnetite or Fe-phosphate to fit the measured EXAFS spectra (Figs 4 and 5, Table 1). These Fe-bearing mineral contents are calculated by multiplying the estimated relative contents by Fe_2O_3 contents measured by XRF (Figs. 5 and 6; Okada et al., 2015).

All the EXAFS spectra show similar strong hematite signature such as two-humped small positive peaks at $k = 5$ and 5.5, large negative amplitudes at $k = 7.2$ and 9.2, and large positive amplitudes at $k = 4.0$, 6.4, 7.6, and 8.6 (Fig. 4). The LCF result shows that more than 50% of Fe-bearing minerals incorporated in these samples were hematite, except for PAK 2 − 9 (Fig. 5; Table 1). The weaker negative amplitude at $k = 8$ and positive amplitude at $k = 8.6$ for PAK 2 − 9 compared to the others resulted in the smaller contribution of hematite (Fig. 4).

The relative abundance of illite is clearly reflected in the EXAFS spectra, although EXAFS oscillation of illite is smaller especially at higher k regions (Fig. 5). For example, the comparison between PAK 2 + 9 and PAK 2 − 3, which contains most and least abundant of illite, respectively, shows that the EXAFS oscillation of PAK 2 + 9 slightly shifted leftward around $k = 6$ and 9 (Fig. 5). The leftward shift of PAK 2 + 9 reflects the peak-top of illite at $k = 6.0$, whereas the PAK 2 − 3 is affected by the peak-top of hematite at $k = 6.4$. Similarly, the negative peak maximum at $k = 9.0$ strongly contributes to the spectrum of PAK 2 + 9, while that of hematite, $k = 9.2$, results in the spectrum of PAK 2 − 3 shifted rightward. In addition, the two-humped peaks at $k = 5$ and 5.5, reflecting hematite signature, of PAK 2 + 9 is relatively flat owing to the flatness of illite signature at that k region, while that of PAK 2 − 3 strongly follows the hematite signature with higher peak at former one.

Relative enrichment of authigenic hematite to detrital hematite was estimated by normalizing the total hematite content by terrigenous materials (illite and Al_2O_3). Their minimum values were the purple chert (PAK 2 + 9; Fig. 6).

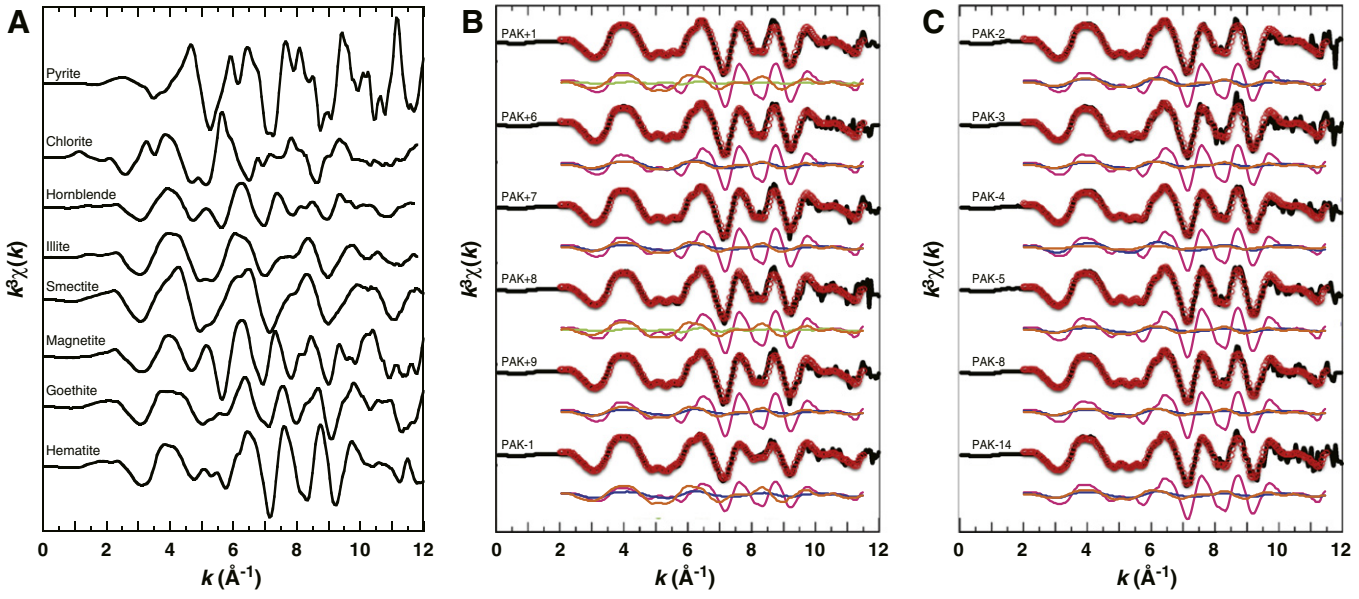

Fig. 4. Iron K-edge EXAFS spectra of (A) standard minerals used to fit the measured chert samples and (B) and (C) chert samples with fitting results and contributions of the end-member mineral components listed in Table 1. The solid black line denotes the measured spectra, and the blue circle shows the results of the fit from Table 1. The colored solid lines show the contributions of each species: blue: the illite fraction: the phosphate fraction, green: the magnetite fraction, and red: the hematite fraction.

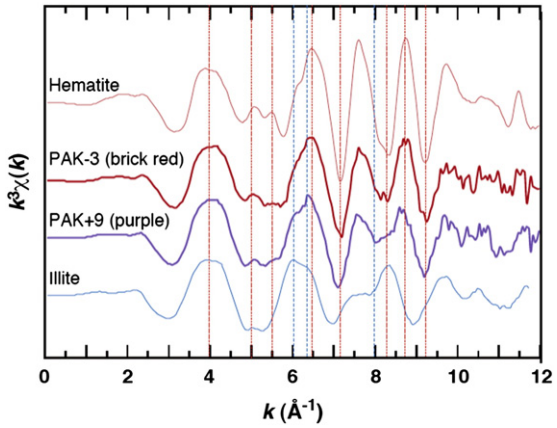

Fig. 5. Iron K-edge EXAFS spectra of standard minerals (hematite and illite) and selected chert samples with highest (PAK-3; brick red chert) and lowest hematite content (PAK + 9; purple chert).

5. Discussion

5.1. Changes in detrital/authigenic hematite burial rate across the end-Triassic extinction event

To understand the paleoclimatic/paleoceanographic changes across the end-Triassic event, here we examine change in the detrital/authigenic origin of hematite in cherts by using XAFS and XRF. The minimum hematite content normalized by terrigenous materials (illite and Al_2O_3) was the purple chert (PAK 2 + 9; Fig. 6), indicating the depletion of authigenic hematite to detrital hematite. Similar decreased hematite content in purple cherts is also reported by using Mössbauer spectroscopy (Kubo et al., 1996; Sato et al., 2012).

The major sources of hematite and other terrigenous material were eolian dust, not riverine input, because the studied section represents a pelagic deep-sea succession in the Panthalassa ocean (Fig. 1). A decrease of detrital hematite could reflect a reduction of silicate weathering rate and/or a weakening global monsoonal climate, because wind-blown dust was likely a major input of terrestrial hematite. However, monsoonal climate and silicate weathering rate would be stronger after the end-Triassic extinction event due to global warming (e.g. Whiteside et al., 2010; Schaller et al., 2012). In addition, the shale thickness increases in this section, suggesting the increased eolian dust input to pelagic Panthalassa. Therefore decreased hematite content implied that decreased authigenic hematite relative to detrital hematite in the purple chert.

There are several ways to reduce authigenic hematite in the ocean: 1) decrease of hematite production by iron bacteria activities (Préat et al., 1999, 2011); and 2) dissolution of authigenic hematite due to changes in ocean redox and/or pH conditions (e.g. Abrajevitch et al., 2013; Isozaki, 1997; Sun et al., 2015). The cause of the dissolution of hematite is still unknown (e.g. pH, organic acids, pressure solution, temperature) and could be related to a non-steady-state early diagenesis under the sea-floor (van der Zee et al., 2005).

The solubility of hematite increases with the decreasing Eh and pH in the ocean (Brookins, 1988; Raiswell and Canfield, 2012), although it is difficult to estimate the exact Eh and pH of deep-ocean sea-water and sediment pore water in the past. Negligible changes in MnO/Al_2O_3 suggested no anoxic condition occurred in the deep-sea across end-Triassic extinction interval (Okada et al., 2015). This idea is supported by other redox sensitive element ratios (U, V, Ni, Cr), and positive Ce anomaly across end-Triassic extinction interval at the Kurusu section, located in the different thrust sheets and several tens of kilometer away from Katsuyama section studied (Hori et al., 2007). The cause of such acidification might have been the drastically increased atmospheric CO_2 across the end-Triassic extinction event on the basis of the stomatal index and pedogenic carbonate proxies (Beerling, 2002; Beerling and Berner, 2002; McElwain et al., 1999; Schaller et al., 2011, 2012; Steinthorsdottir et al., 2011), which could have caused deep-ocean acidification and depletion of dissolved oxygen (e.g., Hotinski et al., 2001; Meyer and Kump, 2008). Therefore, deep-ocean acidification in conjunction with possible Eh drop might have caused the loss of authigenic hematite when purple chert accumulated.

Table 1
The linear combination fitting (LCF) results of Fe K-edge EXAFS and valence state analysis. Py: pyrite; Fa: fayalite; Chl: chlorite; Ill: illite; Sm: smectite; Mag: magnetite; Goet: goethite; Hem: hematite. Note that R (%) is calculated using Eq. (1).

	R factor	Hem	Mag	Pho	Ill	Py	Fa	Chl	Sm
PAK 2 + 1	0.050	55.7%	3.9%	–	40.4%	–	–	–	–
PAK 2 + 6	0.058	56.4%	–	23.7%	19.9%	–	–	–	–
PAK 2 + 7	0.082	54.6%	6.3%	–	39.1%	–	–	–	–
PAK 2 + 8	0.060	56.4%	–	16.1%	27.4%	–	–	–	–
PAK 2 + 9	0.038	37.2%	–	18.2%	44.6%	–	–	–	–
PAK 2 − 1	0.074	54.3%	–	24.4%	21.3%	–	–	–	–
PAK 2 − 2	0.121	61.2%	–	18.6%	20.2%	–	–	–	–
PAK 2 − 3	0.063	59.1%	–	30.8%	10.1%	–	–	–	–
PAK 2 − 4	0.069	50.1%	–	8.3%	41.6%	–	–	–	–
PAK 2 − 5	0.056	64.9%	–	13.8%	21.3%	–	–	–	–
PAK 2 − 8	0.051	61.8%	–	17.4%	20.8%	–	–	–	–
PAK 2 − 14	0.070	58.4%	–	17.0%	24.6%	–	–	–	–

5.2. Timing of deep-ocean acidification across the end-Triassic extinction event

Two acidification stages were proposed from ~100–120 kyr and ~35–50 kyr prior to the end-Triassic extinction level (Abrajevitch et al., 2013). However, the first pulses of the CAMP volcanism were coincident with the end-Triassic extinction of marine biota within 20 kyr (e.g., Deenen et al., 2010; Ruhl and Kürschner, 2011; Whiteside et al., 2010). In addition, ~100 kyr long-term deep-ocean acidification events need protracted CO_2 injection, since ocean acidification could have recovered quickly (~10 kyr) from abrupt CO_2 increase through increased weathering and alkalinity (e.g. Hönisch et al., 2012). On the contrary, the duration of the first pulse of the CAMP volcanism was within 40 kyr, and second pulse was ~300 kyr after the first one on the basis of the high-resolution U–Pb dating and astrochronology of CAMP flood basalts within lacustrine sequences in North America and Africa (e.g. Blackburn et al., 2013; Olsen et al., 1996, 2003; Whiteside et al., 2007). Therefore, two acidification stages of Abrajevitch et al. (2013) are inconsistent with the timing of CAMP volcanism and end-Triassic extinction.

These inconsistencies can be explained by the effect of deep-ocean acidification on sediment pore water (Fig. 8). The deep-ocean acidification could have affected the pH of pore water in deep-sea sediments. The acid pore water would have inhibited the bacterial growth or, alternatively, led to a rapid oxidation of the magnetosomes, preventing their preservation in deep-ocean sediment within a certain depth (Abrajevitch et al., 2013), although the detailed formation process of biogenic magnetite and authigenic hematite are still largely unknown (e.g. Yamazaki and Shimono, 2013). Therefore, the estimated duration of initial and second stages by Abrajevitch et al. (2013) should be considered as the maximum duration. If deep-ocean acidification event occurred just above the purple/dusty red chert boundary, the end-Triassic extinction of radiolarian and conodont was almost synchronous with the deep-ocean acidification event within ~20 kyr (Fig. 7).

5.3. CAMP volcanism and deep-ocean acidification

Timing of the deep-ocean acidification and CAMP volcanism could be inferred by changes in the geochemical characters of cherts in the Inuyama area (Okada et al., 2015). The Fe_2O_3/Al_2O_3, MgO/Al_2O_3, and

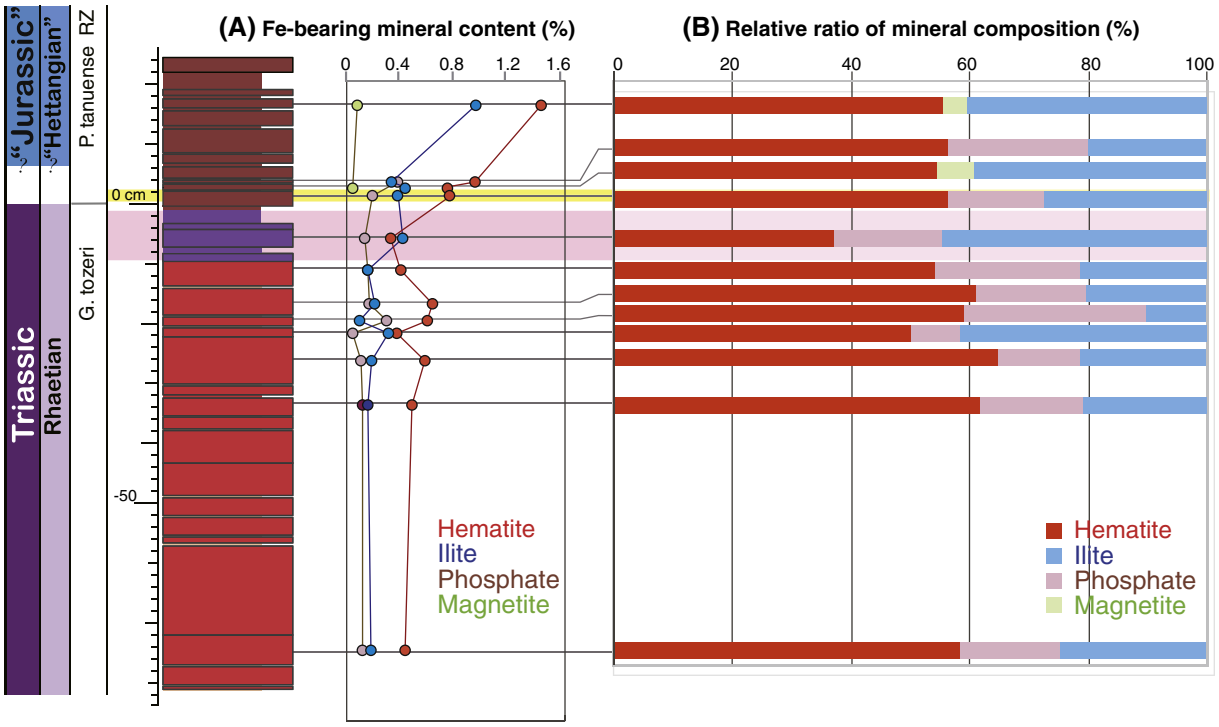

Fig. 6. Stratigraphic changes in (A) Fe-bearing mineral contents and (B) relative ratio of mineral composition of Triassic–Jurassic deep-sea sequence at the Katsuyama section, Inuyama, Japan.

Al_2O_3/SiO_2 ratios increased across the end-Triassic extinction (Fig. 7). These results suggest the possible changes in the aeolian dust composition in cherts, which could have reflected volcanism-induced climate changes.

Primary factor controlling the aeolian dust composition is heterogeneity in composition of the dust source(s) and path(s) (e.g. Schwertmann and Taylor, 1987; Moreno et al., 2006; Lawrence and Neff, 2009; Maher et al., 2010). Changes in the dust source areas could have been caused by changes in wind direction, climate of source regions, and/or appearance/disappearance of source regions (e.g. Lawrence and Neff, 2009; Maher et al., 2010). Across the end-Triassic extinction interval, atmospheric circulation should have changed as increased pCO_2 (e.g. Hasegawa et al., 2012; Toggweiler and Russell, 2008). Shifting climatic conditions have been described from arid to humid or humid to arid, which may be due to shifting the climate belts (Balog et al., 1999; Bonis et al., 2010; Götz et al., 2011). However, it is difficult to reconstruct the spatial variations in rock types of potential dust source regions.

After CAMP volcanism, basalt should be one of the most likely sources of Fe-, Mg-rich aeolian dust for dusty red chert in the Panthalassa, because CAMP flood basalts covered almost one-third area of the low latitude of Pangea (Fig. 1; McHone, 2002; Knight et al., 2004; Nomade et al., 2007). Such distribution is within the modern dust source regions between 15° and 45° (e.g. Prospero et al., 2002). Recently, increased Mg content of tropical terrestrial sequence in Morocco has been interpreted as the increased supply of mafic clay mineral produced from the weathered CAMP basalts (Dal Corso et al., 2014). Our geochemical trend is consistent with the additional aeolian input of Fe-, Mg-rich clay mineral from the weathered CAMP basalts (Fig. 7).

Increased Al_2O_3/SiO_2 across the end-Triassic extinction seems to have reflected the increased dust input to pelagic Panthalassa. Although Al_2O_3/SiO_2 is mixing ratio of terrigenous material and biogenic silica, increased shale thickness across end-Triassic extinction also supports increased dust input. One third of total estimated CAMP basalt volume of the ~3×10^6 km^3 (McHone et al., 2003) could have been weathered within ~2 Ma to explain the pCO_2 falls from an excess of ~4000 ppm to nearly background levels of ~1000 to 2000 ppm (e.g. Schaller et al., 2011a, b, 2012). In addition, CAMP volcanism could have caused not only a great deal of weathered basalts as the origin of aeolian dust, but also expansion of dust source regions due to vegetation collapse (e.g. van de Schootbrugge et al., 2009). These factors could have increased the eolian dust flux into the pelagic Panthalassa.

If onset of the deep-ocean acidification event were ~120 kyr before the end-Triassic extinction (Abrajevitch et al., 2013), the onset of deep-ocean acidification predated the end-Triassic extinction and the increase in eolian dust of the weathered CAMP origin delayed. However, CAMP volcanism started only a few tens of thousands years before the end-Triassic extinction of terrestrial biota (Blackburn et al., 2013; Dal Corso et al., 2014). On the other hand, if the onset of deep-ocean acidification event occurred just before the deposition of dusty red chert, the deep-ocean acidification was synchronous with the end-Triassic extinction and increase in the eolian dust flux (Fig. 7). The latter possibility needs to be assumed the deep-ocean acidification on sediment pore water up to 10 cm (Fig. 8).

Similar lithologic changes in color of cherts are observed mid-Anisian (just after the end-Permian "Superanoxia"; Isozaki, 1997), Carnian (Nakada et al., 2014; Sugiyama, 1997), and mid-Cretaceous (Aptian OAE 1a; Ihoriya et al., 2009). These intervals are also known as the periods of large igneous provinces (Lips) of the prolonged Siberian Trap, Wrangellia, and On Tong Java, respectively (e.g. Wignall, 2001; Furin et al., 2006; Dal Corso et al., 2012). If these purple and dusty red cherts can be used as indicators of paleo-acidification and volcanism events, respectively, the high-resolution lithostratigraphy of deep-sea chert sequences will have potential information on the impact of volcanisms on paleoceanographic/paleoclimatic conditions.

6. Summary

This study examined the deep-ocean acidification and volcanism across the end-Triassic extinction based on the stratigraphic changes of chemical and mineralogical compositions of deep-sea chert. Using XRF and XAFS results, hematite content normalized by terrigenous

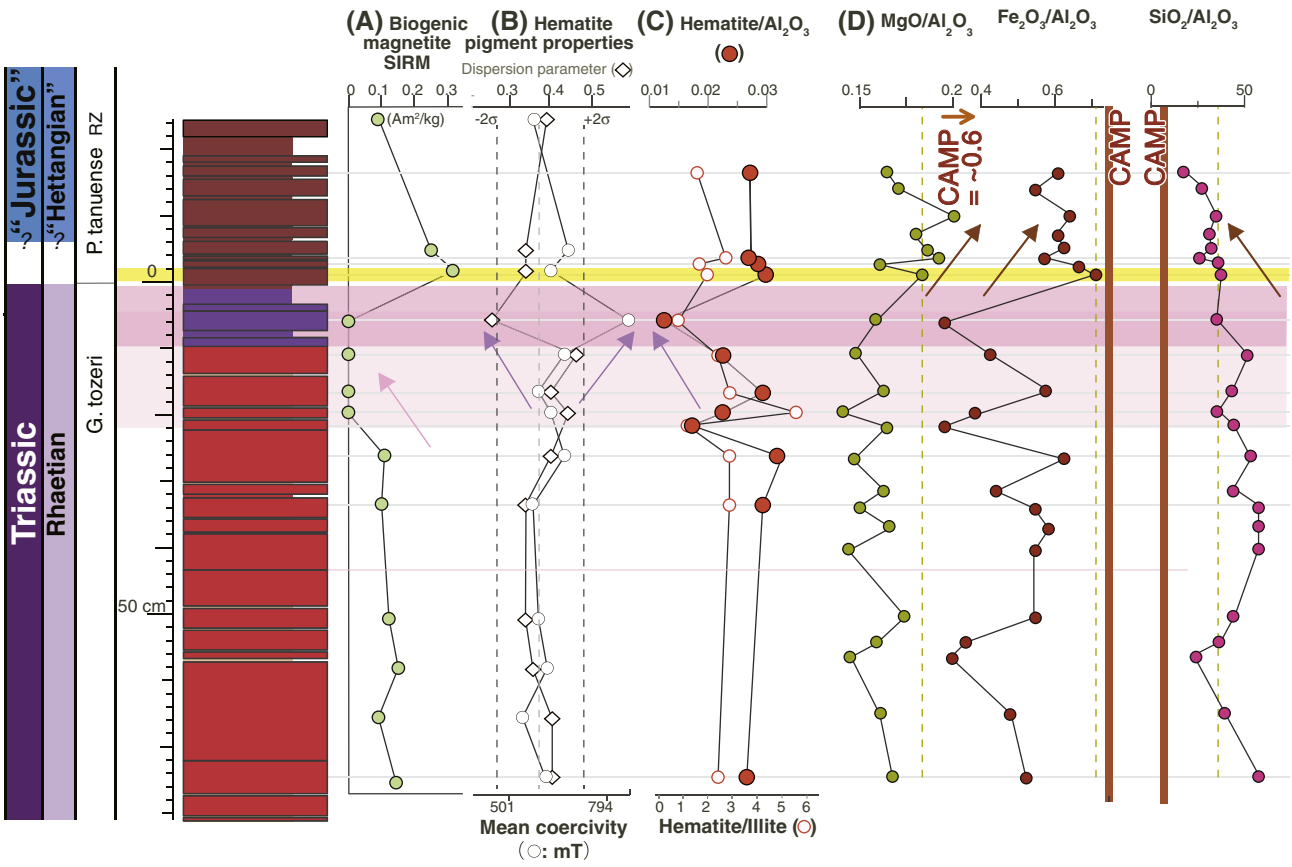

Fig. 7. Stratigraphic changes in magnetic, mineralogical, and geochemical data across the Triassic–Jurassic (T–J) transition at the Katsuyama section, Inuyama, Japan. (A) Biogenic magnetite saturation isothermal remnant magnetization (SIRM; mA m^2/kg) (Abrajevitch et al., 2013). (B) Hematite pigment properties (Mean coercivity (mT, logarithmic scale; open circle) and Dispersion parameter (DP; diamond)). Dashed red lines indicate range of ± 2 standard deviations from mean for both values (Abrajevitch et al., 2013). (C) Hematite/illite (open circle) and hematite/Al_2O_3 (closed circle) (D) MgO/Al_2O_3, Fe_2O_3/Al_2O_3, and SiO_2/Al_2O_3 ratios. Yellow dotted thin line and brown thick lines indicate the chemical compositions of the base of dusty red chert and the Central Atlantic magmatic province (CAMP) basalts (Deenen et al., 2010), respectively.

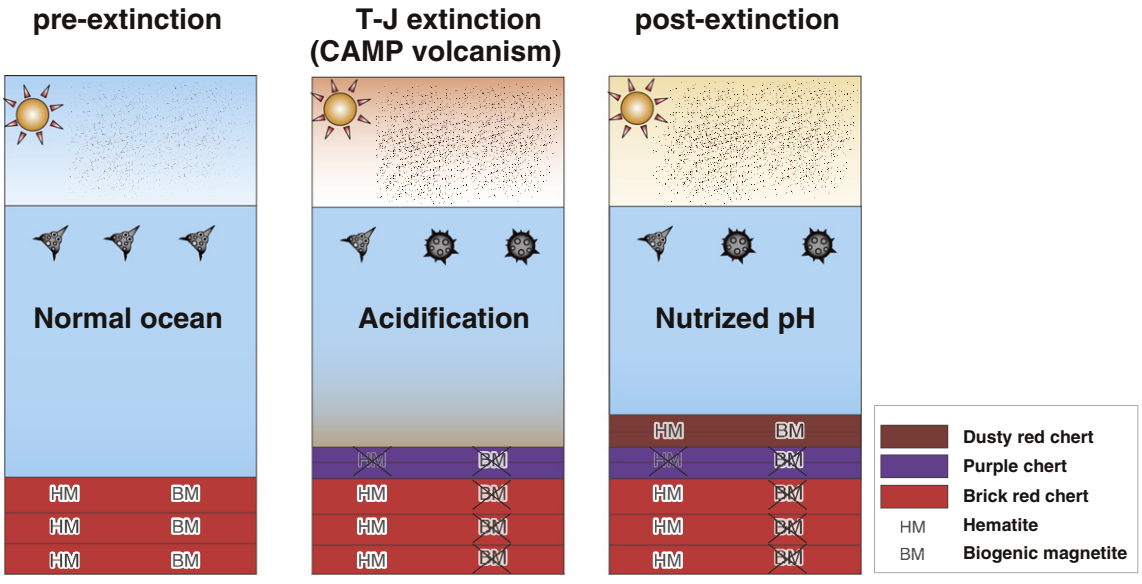

Fig. 8. Schematic illustrations of sedimentary environment in the pelagic Panthalassa through the latest Triassic to earliest Jurassic. (A) pre-extinction mode. Brick red cherts deposited under normal environment with ubiquitous authigenic hematite (HM) and Biogenic magnetite (BM). (B) The Extinction mode with Central Atlantic magmatic province (CAMP). Purple cherts deposited under the deep-ocean acidification and losses of authigenic hematite and biogenic magnetite (marked by X). Possible aeolian dust input from the weathered CAMP basalts results in the increased dust flux, compare to the pre-extinction mode. (C) The post-extinction mode. Dusty red cherts deposited under normal environment with ubiquitous authigenic hematite and biogenic magnetite. Possible aeolian dust input from the weathered CAMP basalts results in the increased dust flux, compare to the pre-extinction mode.

materials (Al_2O_3 and illite) showed minimum at purple chert, just below the end-Triassic extinction level of conodont and faunal turnover of radiolarian fossils. These results suggest that the loss of authigenic hematite within the deep-sea chert, probably due to deep-ocean acidification. Thus, the previously estimated duration of deep-ocean acidification events of ~120 kyr and ~50 kyr (Abrajevitch et al., 2013) should be considered as the maximum duration without considering the acidification of sediment pore water. If the deep-ocean acidification was less than 10 kyr, as estimated by robust numerical models, deep-ocean acidification was almost coincident with the end-Triassic extinction event and CAMP volcanism.

Coincidence between the end-Triassic extinction of radiolaria and conodont in pelagic Panthalassa and CAMP volcanism was inferred from the increased MgO/Al_2O_3, Fe_2O_3/Al_2O_3, and Al_2O_3/SiO_2 ratios across brick red–purple/dusty red chert boundary. These geochemical trends are consistent with the chemical composition of CAMP. Synchrony among them supports possible linkage among CAMP volcanism, deep-ocean acidification, and end-Triassic extinction. Similar purple and dusty red cherts might have potential information on deep-ocean acidification and volcanic events in other geologic events.

Acknowledgments

We thank Peter Baumgartner (Lausanne University), Paul E. Olsen (Columbia University), Morgan Schaller (Rutgers University), David Kemp (Open University), Kazumi Ozaki (University of Tokyo), and Youichi Usui (JAMSTEC) for their critical discussion. The authors are grateful to the associate editor Dr. Paul Hesse, and reviewer Dr. Yadong Sun and two anonymous reviewers for providing suggestions and comments that helped improve the manuscript. The speciation of Fe was performed with the approval of the JASRI (Proposal No. 2013B1658). This research was partly supported by grants from the Japan Society for the Promotion of Science (20127767) awarded to M. Ikeda.

References

Abrajevitch, A., Hori, R.S., Kodama, K., 2013. Rock magnetic record of the Triassic–Jurassic transition in pelagic bedded chert of the Inuyama section, Japan. Geology 41, 803–806.

Ando, A., Kodama, K., Kojima, S., 2001. Low-latitude and Southern Hemisphere origin of Anisian (Triassic) bedded chert in the Inuyama area, Mino terrene, central Japan. J. Geophys. Res. 106, 1973–1986.

Bacon, K.L., Belcher, C.M., Haworth, M., McElwain, J.C., 2013. Increased atmospheric SO_2 detected from changes in leaf physiognomy across the Triassic–Jurassic boundary interval of East Greenland. Plos One 8 (4), 1–12.

Balog, A., Read, J.F., Haas, J., 1999. Climate-controlled early dolomite, Late Triassic cyclic platform carbonates, Hungary. J. Sediment. Res. 69, 267–282.

Beerling, D., 2002. CO_2 and the end-Triassic mass extinction. Nature 415 (6870), 386–387.

Beerling, D.J., Berner, R.A., 2002. Biogeochemical constraints on the Triassic–Jurassic boundary carbon cycle event. Glob. Biogeochem. Cycles 16, 1–13. http://dx.doi.org/10.1029/2001GB001637.

Blackburn, T.J., Olsen, P.E., Bowring, S.A., McLean, N.M., Kent, D.V., Puffer, J., McHone, G., Rasbury, E.T., Et-Touhami, M., 2013. Zircon U–Pb geochronology links the end-Triassic extinction with the Central Atlantic magmatic province. Science 340, 941–945.

Bonis, N.R., Ruhl, M., Kürschner, W.M., 2010. Milankovitch-scale palynological turnover across the Triassic–Jurassic transition at St. Audrie's Bay, SW UK. J. Geol. Soc. 167, 877–888.

Brookins, D.G., 1988. Eh-pH Diagrams for Geochemistry. Springer-Verlag, p. 176.

Carter, E.S., Hori, R.S., 2005. Global correlation of the radiolarian faunal change across the Triassic–Jurassic boundary. Can. J. Earth Sci. 42, 777–790.

Carter, E.S., Goričan, Š., Guex, J., O'Dogherty, L., De Wever, P., Dumitrica, P., Hori, R.S., Matsuoka, A., Whalen, P.A., 2010. Global radiolarian zonation for the Pliensbachian, Toarcian and Aalenian. Palaeogeogr. Palaeoclimatol. Palaeoecol. 297, 401–419.

Dal Corso, J., Mietto, P., Newton, R.J., Pancost, R.D., Preto, N., Roghi, G., Wignall, P.B., 2012. Discovery of a major negative δ13C spike in the Carnian (Late Triassic) linked to the eruption of Wrangellia flood basalts. Geology 40, 79–82. http://dx.doi.org/10.1130/G32473.1.

Dal Corso, J., Marzoli, A., Tateo, F., Jenkyns, H.C., Bertrand, H., Youbi, N., Mahmoudi, A., Font, E., Burati, N., Cirili, S., 2014. The dawn of CAMP volcanism and its bearing on the end-Triassic carbon cycle disruption. J. Geol. Soc. Lond. 171, 153–164.

Deenen, M.H.L., Ruhl, M., Bonis, N.R., Krijgsman, W., Kuerschner, W.M., Reitsma, M., van Bergen, M.J., 2010. A new chronology for the end-Triassic mass extinction. Earth Planet. Sci. Lett. 291, 113–125.

Furin, S., Preto, N., Rigo, M., Roghi, G., Gianolla, P., Crowley, J.L., Bowring, S.A., 2006. High-precision U–Pb zircon age from the Triassic of Italy: implications for the Triassic time scale and the Carnian origin of calcareous nannoplankton and dinosaurs. Geology 34, 1009–1012.

Götz, A., Ruckwied, K., Barbacka, M., 2011. Palaeoenvironment of the Late Triassic (Rhaetian) and Early Jurassic (Hettangian) Mecsek coal formation (south Hungary): implications from macro- and microfloral assemblages. Palaeobiodiversity Palaeoenvironments 91, 75–88.

Greene, S.E., Martindale, R.C., Ritterbush, K.A., Bottjer, D.J., Corsetti, F.A., Berelson, W.M., 2012. Recognising ocean acidification in deep time: an evaluation of the evidence for acidification across the Triassic–Jurassic boundary. Earth Sci. Rev. 113, 72–93.

Guex, J., Bartolini, A., Atudorei, V., Taylor, D., 2004. High-resolution ammonite and carbon isotope stratigraphy across the Triassic–Jurassic boundary at New York Canyon (Nevada). Earth Planet. Sci. Lett. 225, 29–41.

Guex, J., Bartolini, A., Taylor, D., Atudorei, V., Thelin, P., Bruchez, S., Tanner, L.H., Lucas, S.G., 2008. The organic carbon isotopic and paleontological record across the Triassic–Jurassic boundary at the candidate GSSP section at Ferguson Hill, Muller Canyon, Nevada, USA: Comment. Palaeogeogr. Palaeoclimatol. Palaeoecol. 273, 205–206.

Guex, J., Schoene, B., Bartolini, Spangenberg, J., Schaltegger, U., O'Dogherty, L., Taylor, D., Bucher, H., Atudorei, V., 2012. Geochronological constraints on post-extinction recovery of the ammonoids and carbon cycle perturbations during the Early Jurassic. Palaeogeogr. Palaeoclimatol. Palaeoecol. 346–347, 1–11.

Hallam, A., 2002. How catastrophic was the end-Triassic mass extinction? Lethaia 35, 147–157.

Hasegawa, H., Tada, R., Jiang, X., Suganuma, Y., Imsamut, S., Charusiri, P., Ichinnorov, N., Khand, Y., 2012. Drastic shrinking of the Hadley circulation during the mid-Cretaceous supergreenhouse. Clim. Past 8, 1323–1337.

Higuchi, Y., Hori, R.S., 1996. Sample preparation of siliceous rocks for quantitative analysis of trace elements by X-ray fluorescence method. Mem. Fac. Sci. Ehime Univ. 2, 1–14 (in Japanese with English abstract).

Hönisch, B., Ridgwell, A., Schmidt, D.N., Thomas, E., Gibbs, S.J., Sluijs, A., Zeebe, R., Kump, L., Martindale, R.C., Greene, S.E., Kiessling, W., Ries, J., Zachos, J.C., Royer, D.L., Barker, S., Marchitto Jr., T.M., Moyer, R., Pelejero, C., Ziveri, P., Foster, G.L., Williams, B., 2012. The Geological Record of Ocean Acidification. Science 355, 1058–1063.

Hori, R., 1988. Some characteristic radiolarians from Lower Jurassic bedded cherts of the Inuyama area. Southwest Japan. Trans. Proc. Palaeont. Soc. Japan N. S. 151, 543–563.

Hori, R., 1990. Lower Jurassic radiolarian zones of SW Japan. Trans. Proc. Paleontol. Soc. Jpn N.S. 159, 562–586.

Hori, R., 1992. Radiolarian biostratigraphy at the Triassic–Jurassic Period boundary in bedded cherts from the Inuyama area, central Japan. J. Geosci. Osaka City Univ. 35, 53–65.

Hori, R.S., Higuchi, Y., 1996. Quantitative analysis of trace elements in rock samples by X-ray fluorescence spectrometry, using Rh anode tube. Mem. Fac. Sci. Ehime Univ. 2, 27–36 (in Japanese with English abstract).

Hori, S.R., Cho, C., Umeda, H., 1993. Origin of cyclicity in Triassic–Jurassic radiolarian bedded cherts of the Mino accretionary complex from Japan. Island Arc 3, 170–180.

Hori, S.R., Higuchi, Y., Fujiki, T., 2000. Chemical composition and their environmental records of bedded cherts from accretionary complexes in Japan. Mem. Geol. Soc. Jpn. 55, 43–59 (in Japanese).

Hori, R.S., Fujiki, T., Inoue, E., Kimura, J.I., 2007. Platinum group element anomalies and bioevents in the Triassic–Jurassic deep-sea sediments of Panthalassa. Palaeogeogr. Palaeoclimatol. Palaeoecol. 244, 391–406. http://dx.doi.org/10.1016/j.palaeo.2006.06.038.

Hotinski, R.M., Bice, K.L., Kump, L.R., Najjar, R.G., Arthur, M.A., 2001. Ocean stagnation and end-Permian anoxia. Geology 29, 7–10.

Ihoriya, N., Hori, R.E., Ikehara, M., 2009. Constraints upon anoxic water mass and variations in carbon isotopes during OAE1a (Early Cretaceous) from deep-sea sedimentary rocks of the Pacific Ocean. News Osaka Micropaleontol. 14, 297–315.

Ikeda, M., Hori, S.R., 2014. Effects of Karoo–Ferrar volcanism and astronomical cycles on the Toarcian oceanic anoxic events (Early Jurassic). Palaeogeogr. Palaeoclimatol. Palaeoecol. 410, 134–142.

Ikeda, M., Tada, R., 2013. Long period astronomical cycles from the Triassic to Jurassic bedded chert sequence (Inuyama, Japan); geologic evidences for the chaotic behavior of Solar planets. Earth Planets Space 65, 1–10.

Ikeda, M., Tada, R., 2014. A 70 million year astronomical time scale for the deep-sea bedded chert sequence (Inuyama, Japan): Implications for the Triassic–Jurassic geochronology. Earth Planet. Sci. Lett. 399, 30–43.

Ikeda, M., Tada, R., Sakuma, H., 2010. Astronomical cycle origin of bedded chert; middle Triassic bedded chert sequence, Inuyama, Japan. Earth Planet. Sci. Lett. 297, 369–378.

Isozaki, Y., 1997. Permo-Triassic boundary superanoxia and stratified superocean; records from lost deep sea. Science 276, 235–238.

Kent, D.V., Tauxe, L., 2005. Corrected Late Triassic Latitudes for Continents Adjacent to the North Atlantic. Science 307, 240–244. http://dx.doi.org/10.1126/science.1105826.

Kimura, K., Hori, R., 1993. Offscraping accretion of Jurassic chert-clastic complexes in the Mino-Tamba Belt, central Japan. J. Struct. Geol. 15, 145–161.

Knight, K.B., Nomade, S., Renne, P.R., Marzoli, A., Bertrand, H., Youbi, N., 2004. The Central Atlantic magmatic province at the Triassic–Jurassic boundary: paleomagnetic and $^{40}Ar/^{39}Ar$ evidence from Morocco for brief, episodic volcanism. Earth Planet. Sci. Lett. 228, 16–143.

Kubo, K., Isozaki, Y., Matsuo, M., 1996. Color of bedded chert and redox condition of depositional environment: ^{57}Fe Mössbauer spectroscopic study on chemical state of iron in Triassic deep-sea pelagic chert. J. Geol. Soc. Jpn. 102, 40–48 (in Japanese with English abstract).

Lawrence, C.L., Neff, J.C., 2009. The contemporary physical and chemical flux of aeolian dust: a synthesis of direct measurements of dust deposition. Chem. Geol. 267, 46–63.

Maher, B.A., Prospero, J.M., Mackie, D., Gaiero, D., Hesse, P.P., Balkanski, Y., 2010. Global connections between aeolian dust, climate and ocean biogeochemistry at the present day and at the last glacial maximum. Earth Sci. Rev. 99, 61–97.

Marzoli, A., Renne, P.R., Piccirillo, E.M., Ernesto, M., Bellieni, G., De Min, A., 1999. Extensive 200-million-year-old continental flood basalts of the Central Atlantic magmatic province. Science 284 (5414), 616–618.

Matsuda, T., Isozaki, Y., 1991. Well-documented travel history of Mesozoic pelagic chert in Japan: from remote ocean to subduction zone. Tectonics 10, 475–499.

McElwain, J.C., Beerling, D.J., Woodward, F.I., 1999. Fossil plants and global warming at the Triassic–Jurassic boundary. Science 285 (5432), 1386–1390.

McHone, J.G., 2002. Volatile emissions from Central Atlantic magmatic province basalts: mass assumptions and environmental consequences. AGU Monogr. 1–13.

McHone, J.G., et al., 2003. Volatile emissions from the Central Atlantic magmatic province basalts: mass assumptions and environmental consequences. In: Hames, W. (Ed.), The Central Atlantic Magmatic Province: Insights From Fragments of Pangea: Volume Geophysical Monograph, 136. American Geophysical Union, Washington DC.

Meyer, K.M., Kump, L.R., 2008. Oceanic euxinia in Earth history: causes and consequences. Annu. Rev. Earth Planet. Sci. 36, 251–288.

Moreno, T., Querol, X., Castillo, S., Alastuey, A., Cuevas, E., Herrmann, L., Mounkaila, M., Elvira, J., Gibbons, W., 2006. Geochemical variations in aeolian mineral particle from the Sahara–Sahel dust corridor. Chemosphere 65, 261–270.

Murray, R.W., Tenbrink, M.R.B., Gerlach, D.C., Russ, G.P., Jones, D.L., 1991. Rare earth, major, and trace elements in chert from the Franciscan Complex and Monterey Group, California: Assessing REE sources to fine-grainedmarine sediments. Geochim. Cosmochim. Acta 55, 1875–1895.

Murray, R.W., 1994. Chemical criteria to identify the depositional environment of chert: general principles and applications. Sediment. Geol. 90, 213–232.

Nakada, R., Ogawa, K., Suzuki, N., Takahashi, S., Takahashi, Y., 2014. Late Triassic compositional changes of aeolian dusts in the pelagic Panthalassa: response to the continental climatic change. Palaeogeogr. Palaeoclimatol. Palaeoecol. 393, 61–75. http://dx.doi.org/10.1016/j.palaeo.2013.10.014.

Nomade, S., Knight, K.B., Beutel, E., Renne, P.R., Verati, C., Féraud, G., Marzoli, A., Youbi, N., Bertrand, H., 2007. Chronology of the Central Atlantic magmatic province: implications for the Central Atlantic rifting processes and the Triassic–Jurassic biotic crisis. Palaeogeogr. Palaeoclimatol. Palaeoecol. 244, 326–344.

O'Day, P.A., Rivera Jr., N., Root, R., Carroll, S.A., 2004. X-ray absorption spectroscopic study of Fe reference compounds for the analysis of natural sediments. Am. Mineral. 89, 572–585.

Oda, H., Suzuki, H., 2000. Paleomagnetism of Triassic and Jurassic red bedded chert of the Inuyama area, central Japan. J. Geophys. Res. 105, 743–767.

Okada, Y., Hori, S.R., Ikeda, M., Ikehara, M., 2015. Geochemical study of Panthalassa deep-sea sedimentary rocks across the Triassic–Jurassic boundary. News Osaka Micropaleontol. 15, 219–232.

Olsen, P.E., Schlische, R.W., Fedosh, M.S., 1996. 580 ky duration of the early Jurassic flood basalt event in eastern North America estimated using Milankovitch cyclostratigraphy. In: Morales, M. (Ed.), The Continental Jurassic: Flagstaff, Museum of Northern Arizona Bulletin. 60, pp. 11–22.

Olsen, P.E., Kent, D.V., Et-Touhami, M., Puffer, J., 2003. Cyclo-, magneto-, and biostratigraphic constraints on the duration of the CAMP event and its relationship to the Triassic–Jurassic boundary. In: Hames, et al. (Eds.), The Central Atlantic Magmatic Province: Insights From Fragments of Pangea: Volume Geophysical Monograph. 136, pp. 7–32 (Washington DC).

Orchard, M.J., Carter, E.S., Lucas, S.G., Taylor, D.G., 2007. Rhaetian (Upper Triassic) conodonts and radiolarians from New York Canyon, Nevada, USA. Albertiana 35, 59–65.

Préat, A., Mamet, B., Bernard, A., Gillan, D., 1999. Bacterial mediation, red matrices diagenesis, Devonian, Montagne Noire (southern France). Sediment. Geol. 126, 223–242.

Prospero, J.M., Ginoux, P., Torres, O., Nicholson, S.E., Gill, T.E., 2002. Environmental characterization of global sources of atmospheric soil dust identified with the NIMBUS 7 total ozone mapping spectrometer (TOMS) absorbing aerosol product. Rev. Geophys. 40.

Raiswell, R., Canfield, D., 2012. The iron biogeochemical cycle past and present. Geochem. Perspect. 1, 1–215.

Raup, D.M., Sepkoski Jr., J.J., 1982. Mass extinctions in the marine fossil record. Science 215, 1501–1503. http://dx.doi.org/10.1126/science.215.4539.1501.

Ravel, B., Newville, M., 2005. Athena, artemis, hephaestus: data analysis for X-ray absorption spectroscopy using IFEFFIT. J. Synchrotron Radiat. 12, 537–541.

Ruhl, M., Kürschner, W.M., 2011. Multiple phases of carbon cycle disturbance from large igneous province formation at the Triassic–Jurassic transition. Geology 39, 431–434. http://dx.doi.org/10.1130/G31680.1.

Sato, T., Isozaki, Y., Shozugawa, K., Seimiya, K., Matsuo, M., 2012. ^{57}Fe Mössbauer analysis of the Upper Triassic–Lower Jurassic deep-sea chert: paleo-redox history across the Triassic–Jurassic boundary and the Toarcian oceanic anoxic event. Hyperfine Interact. http://dx.doi.org/10.1007/s10751-011-0520-4.

Schaller, M.F., Wright, J.D., Kent, D.V., 2011. Atmospheric pCO_2 perturbations associated with the Central Atlantic magmatic province. Science 331, 1404–1409.

Schaller, M.F., Wright, J.D., Kent, D.V., Olsen, P.E., 2012. Rapid emplacement of the Central Atlantic magmatic province as a net sink for CO_2. Earth Planet. Sci. Lett. 323–324, 27–39.

Schaltegger, U., Guex, J., Bartolini, A., Schoene, B., Ovtcharova, M., 2008. Precise U-Pb age constraints for end-Triassic mass extinction, its correlation to volcanism and Hettangian post-extinction recovery: Earth Planet. Sci. Lett. 267, 266–275. http://dx.doi.org/10.1016/j.epsl.2007.11.031.

Schoene, B., Guex, J., Bartolini, A., Schaltegger, U., Blackburn, T., 2010. Correlating the end-Triassic mass extinction and flood basalt volcanism at the 100000-year level. Geology 38, 387–390.

Schwertmann, U., Taylor, R.M., 1987. Iron oxides. In: Dixon, J.B., Weed, S.B. (Eds.), Minerals in Soil Environments, 2nd ed. Soil Science Society of America, Madison.

Schwertmann, U., Cornell, R.M., 2000. Iron Oxides in the Laborator. 2nd ed. Wiley-VCH.

Scotese, C.R., Langford, R., 1995. 1995, Pangea and the paleogeography of the Permian. In: Scholle, P.A., Peryt, T.M., Ilmer-Scholle, D.S. (Eds.), The Permian of Northern Pangea vol. 1. Springer-Verlag, Berlin, pp. 3–19.

Shibuya, H., Sasajima, S., 1986. Paleomagnetism of red cherts: a case study in the Inuyama area, central Japan. J. Geophys. Res. 91, 105–116.

Steinthorsdottir, M., Jeram, A.J., McElwain, J.C., 2011. Extremely elevated CO_2 concentrations at the Triassic/Jurassic boundary. Palaeogeogr. Palaeoclimatol. Palaeoecol. 308 (3–4), 418–432.

Sugiyama, K., 1997. Triassic and Lower Jurassic radiolarian biostratigraphy in the siliceous claystone and bedded chert units of the southeastern Mino Terrane. Cent. Jpn. Bull. Mizunami Fossil Mus. 24, 79–193.

Sun, Y.D., Wignall, P.B., Joachimski, M.M., Bond, D.P.G., Grasby, S.E., Sun, S., Yan, C.B., Wang, L.N., Chen, Y.L., Lai, X.L., 2015. High amplitude redox changes in the late Early Triassic of South China and the Smithian/Spathian extinction. Palaeogeogr. Palaeoclimatol. Palaeoecol. 427, 62–78.

Tanner, L.H., Lucas, S.G., Chapman, M.G., 2004. Assessing the record and causes of Late Triassic extinctions. Earth Sci. Rev. 65, 103–139.

Tipper, H.W., Guex, J., 1994. Preliminary remarks on the Hettangian ammonite succession in Queen Charlotte Islands, British Columbia. In: Cariou, E., Hantzperque, P. (Eds.), 3rd International Symposium on Jurassic Stratigraphy, Poitiers, France, 1991. Geobios, Mémoire Spécial. 17, pp. 477–483.

Toggweiler, J.R., Russell, J., 2008. Ocean circulation in a warming climate. Nature 451, 286–288.

van de Schootbrugge, B., Quan, T.M., Lindstro¨m, S., Pu¨ttmann, W., Heunisch, C., 2009. Floral changes across the Triassic/Jurassic boundary linked to flood basalt volcanism. Nat. Geosci. 2, 589–594.

van der Zee, C., Slomp, C.P., Rancourt, D.G., de Lange, G.J., van Raaphorst, W., 2005. A Mössbauer spectroscopic study of the iron redox transition in eastern Mediterranean sediments. Geochim. Cosmochim. Acta 69, 441–453.

Voegelin, A., Kaegi, R., Frommer, J., Vantelon, D., Hug, S.J., 2010. Effect of phosphate, silicate, and Ca on Fe(III)-precipitates formed in aerated Fe(II)- and As(III)-containing water studied by X-ray absorption spectroscopy. Geochim. Cosmochim. Acta 74, 164–186.

Wakita, K., 1988. Origin of chaotically mixed rock bodies in the Early Jurassic to Early Cretaceous sedimentary complex of the Mino Terrane, central Japan. Bull. Geol. Surv. Jpn 39, 675–757.

Ward, P.D., Haggart, J.W., Carter, E.S., Wilbur, D., Tipper, H.W., Evans, T., 2001. Sudden productivity collapse associated with the Triassic–Jurassic boundary mass extinction. Science 292, 1148–1151.

Ward, P.D., Garrison, G.H., Haggart, J.W., Kring, D.A., Beattie, M.J., 2004. Isotopic evidence bearing on Late Triassic extinction events, Queen Charlotte Islands, British Columbia, and implications for the duration and cause of the Triassic/Jurassic mass extinction. Earth Planet. Sci. Lett. 224, 589–600.

Ward, P.D., Garrison, G.H., Williford, K.H., Kring, D., Goodwin, D., Beattie, M., McRoberts, C., 2007. The organic carbon isotopic and paleontological record across the Triassic–Jurassic boundary at the candidate GSSP section at Ferguson Hill, Muller Canyon, Nevada, USA. Palaeogeogr. Palaeoclimatol. Palaeoecol. 244, 279–287.

Whiteside, J.H., Olsen, P.E., Kent, D.V., Fowell, S.J., Et-Touhami, M., 2007. Synchrony between the Central Atlantic magmatic province and the Triassic–Jurassic mass-extinction vent? Palaeogeogr. Palaeoclimatol. Palaeoecol. 244, 345–367.

Whiteside, J.H., Olsen, P.E., Eglinton, T., Brookfield, M.E., Sambrotto, R.N., 2010. Compound-specific carbon isotopes from Earth's largest flood basalt eruptions directly linked to the end-Triassic mass extinction. Proc. Natl. Acad. Sci. 107, 6721–6725.

Wignall, P.B., 2001. Large igneous provinces and mass extinctions. Earth Sci. Rev. 53, 1–33.

Williford, K.H., Ward, P.D., Garrison, G.H., Buick, R., 2007. An extended organic carbon-isotope record across the Triassic–Jurassic boundary in the Queen Charlotte Islands, British Columbia, Canada. Palaeogeogr. Palaeoclimatol. Palaeoecol. 244, 290–296.

Yamazaki, T., Shimono, T., 2013. Abundant bacterial magnetite occurrence in oxic red clay. Geology 41, 1191–1194. http://dx.doi.org/10.1130/G34782.1.

Yao, A., Matsuda, T., Isozaki, Y., 1980. Triassic and Jurassic radiolarians from the Inuyma area, central Japan. J. Geosci. Osaka City Univ. 23, 135–154.

Yoshizaki, T., Tamura, Y., Sakae, S., Hori, R., Komatsu, M., 1996. X-ray fluorescence analysis of major elements for silicate rocks. Mem. Fac. Sci. Ehime Univ. 2, 15–25 (in Japanese with English abstract).